PAPER

Influence of high-permeability discs in an axisymmetric model of the Cadarache dynamo experiment

To cite this article: A Giesecke *et al* 2012 *New J. Phys.* **14** 053005

View the article online for updates and enhancements.

Related content

- Magnetic material in mean-field dynamos driven by small scale helical flows
  A Giesecke, F Stefani and G Gerbeth

- Effect of magnetic boundary conditions on the dynamo threshold of von Kármán swirling flows
  C. Gissinger, A. Iskakov, S. Fauve et al.

- Direct numerical simulation of the axial dipolar dynamo in the Von Kármán Sodium experiment
  C. Nore, D. Castanon Quiroz, L. Cappanera et al.

Recent citations

- Numerical simulation of the von Kármán sodium dynamo experiment
  C. Nore *et al*

- The DRESDYN project: liquid metal experiments on dynamo action and magnetorotational instability
  F. Stefani *et al*

- Effect of fluctuations on mean-field dynamos
  A. Alexakis *et al*

Influence of high-permeability discs in an axisymmetric model of the Cadarache dynamo experiment

A Giesecke[1,6], **C Nore**[2,3], **F Stefani**[1], **G Gerbeth**[1], **J Léorat**[4], **W Herreman**[2,3], **F Luddens**[2] and **J-L Guermond**[2,5]

[1] Helmholtz-Zentrum Dresden-Rossendorf, PO Box 510119, 01314 Dresden, Germany
[2] Laboratoire d'Informatique pour la Mécanique et les Sciences de l'Ingénieur, CNRS, BP 133, 91403 Orsay cedex, France
[3] Université Paris Sud 11, 91405 Orsay cedex, France
[4] Luth, Observatoire de Paris-Meudon, place Janssen, 92195 Meudon, France
[5] Department of Mathematics, Texas A&M University 3368 TAMU, College Station, TX 77843, USA
E-mail: a.giesecke@hzdr.de

Abstract. Numerical simulations of the kinematic induction equation are performed on a model configuration of the Cadarache von-Kármán-sodium dynamo experiment. The effect of a localized axisymmetric distribution of relative permeability μ_r that represents soft iron material within the conducting fluid flow is investigated. The critical magnetic Reynolds number Rm^c for dynamo action of the first non-axisymmetric mode roughly scales like $Rm^c_{\mu_r} - Rm^c_\infty \propto \mu_r^{-1/2}$, i.e. the threshold decreases as μ_r increases. This scaling law suggests a skin effect mechanism in the soft iron discs. More important with regard to the Cadarache dynamo experiment, we observe a purely toroidal axisymmetric mode localized in the high-permeability discs which becomes dominant for large μ_r. In this limit, the toroidal mode is close to the onset of dynamo action with a (negative) growth rate that is rather independent of the magnetic Reynolds number. We qualitatively explain this effect by paramagnetic pumping at the fluid/disc interface and propose a simplified model that quantitatively reproduces numerical results. The crucial role of

[6] Author to whom any correspondence should be addressed.

IOP Institute of Physics **Φ** DEUTSCHE PHYSIKALISCHE GESELLSCHAFT

the high-permeability discs in the mode selection in the Cadarache dynamo experiment cannot be inferred from computations using idealized pseudo-vacuum boundary conditions ($\boldsymbol{H} \times \boldsymbol{n} = 0$).

Contents

1. Introduction

Astrophysical magnetic fields are a ubiquitous phenomenon. They affect the formation and behavior of galaxies, stars or planets and might even be important for structure formation on cosmic scales. On astrophysical scales, fluid flow-driven field generation by virtue of the dynamo effect is relatively uncomplicated because the magnetic Reynolds number is always large. However, due to their limited size the realization of dynamo action in laboratory experiments is a demanding task and requires an elaborate design that makes use of optimizations such as ideal guidance of a fluid flow or a selective choice of materials. Material properties such as electrical conductivity or relative permeability have always been important for experimental dynamos. For example, the use of soft iron in the dynamo experiments of Lowes and Wilkinson (1963,1968) was crucial for the occurrence of magnetic self-excitation. More recently, the addition of high permeability material (soft iron spheres) into a conducting fluid was examined to test magnetic self-excitation (Dobler *et al* 2003) in a flow that otherwise would not be able to sustain a dynamo.

The study presented here was motivated by the Cadarache von-Kármán-sodium (VKS) dynamo (Monchaux *et al* 2007). In this experiment, liquid sodium contained in a cylindrical vessel is driven by two counter-rotating impellers that are located close to the lids of the vessel. Dynamo action is obtained only when (at least one of) the flow-driving impellers are made of soft iron with a relative permeability $\mu_r \approx 65$ (Verhille *et al* 2010). Moreover, the observed magnetic field is dominated by an axisymmetric mode (Monchaux *et al* 2009). It can be conjectured that the occurrence of dynamo action with soft iron impellers and the axisymmetry of the magnetic field are interlinked, but the very nature of the axisymmetric dynamo is still unknown.

A well-known necessary condition for the occurrence of dynamo action is a sufficiently complex conducting fluid flow that couples the toroidal and poloidal components of the

IOP Institute of Physics Φ DEUTSCHE PHYSIKALISCHE GESELLSCHAFT

magnetic field[7]. The interaction between these components gives rise to the so-called dynamo cycle, which consists in regenerating the toroidal field from the poloidal field and vice versa. This coupling can take place on large scales (Dudley and James 1989) as well as on small scales by virtue of the well-known α-effect (Krause and Rädler 1980). It is less well known that non-homogeneities in the electrical conductivity can also introduce such a coupling and, by this, favor dynamo action. For example, a uniform flow over an infinite plate with varying conductivity can produce dynamo action (Busse and Wicht 1992, Wicht and Busse 1993). It is likely that inhomogeneous magnetic permeability can also lead to dynamo action.

In this paper, we investigate the impact of a localized disc-like permeability distribution embedded in a conducting axisymmetric fluid flow on the growth rates of the axisymmetric and first non-axisymmetric magnetic eigenmodes. Induction effects due to non-axisymmetric perturbations (turbulence, small-scale or large-scale flow or conductivity/permeability distributions) are not taken into account. Firstly, we briefly re-examine the threshold of the equatorial dipole mode as in Giesecke *et al* (2010c) and propose an explanation for the scaling law that relates the critical magnetic Reynolds number to the permeability in the impeller discs. Secondly, we investigate the influence of the concentrated high permeability on the axisymmetric field modes. Even though they are always damped, according to Cowling's theorem (Cowling 1933, Hide and Palmer 1982), for large $\mu_{\rm r}$ we find a dominant toroidal mode very close to the onset of dynamo action. We suggest that this eigenmode plays a significant role in the dominance of the axisymmetric mode in the dynamo observed in the VKS experiment (Monchaux *et al* 2007).

2. The model

The induction equation with non-uniform material coefficients, i.e. spatially dependent electrical conductivity $\sigma = \sigma(\boldsymbol{r})$ and relative permeability $\mu_{\rm r} = \mu_{\rm r}(\boldsymbol{r})$, reads

$$\frac{\partial \boldsymbol{B}}{\partial t} = \nabla \times \left(\boldsymbol{u} \times \boldsymbol{B} + \frac{1}{\mu_{\rm r}\mu_0\sigma} \frac{\nabla \mu_{\rm r}}{\mu_{\rm r}} \times \boldsymbol{B} - \frac{1}{\mu_{\rm r}\mu_0\sigma} \nabla \times \boldsymbol{B} \right), \tag{1}$$

where $\boldsymbol{u}$ is the prescribed (mean) flow, $\boldsymbol{B}$ the magnetic flux density and μ_0 the vacuum permeability $(\mu_0 = 4\pi \times 10^{-7}\,{\rm V\,s\,(A\,m)^{-1}})$. The middle term in the right-hand side of equation (1) proportional to $\sim \nabla \mu_{\rm r} \times \boldsymbol{B}$ represents the so-called 'paramagnetic pumping' (Dobler *et al* 2003). This term is responsible for the suction of the magnetic field into the regions with large permeability and involves a (non-divergence-free) velocity-like field that we henceforth call 'pumping velocity'

$$\boldsymbol{V}^\mu = \frac{1}{\mu_{\rm r}\mu_0\sigma} \frac{\nabla \mu_{\rm r}}{\mu_{\rm r}}. \tag{2}$$

The eigenvalue problem associated with equation (1) is solved numerically by using two different methods. One is based on a spectral/finite element approach described in Guermond *et al* (2011) (SFEMaNS, spectral/finite element method for Maxwell and Navier–Stokes equations), which solves the eigenvalue problem using ARPACK. The second approach utilizes a combined finite volume/boundary element method for time-stepping equation (1) (Giesecke

---

[7] In the following, toroidal and poloidal components always refer to the axisymmetric case so that the toroidal component corresponds to the azimuthal field $\boldsymbol{B}_{\rm tor} = B_\varphi \boldsymbol{e}_\varphi$ and the poloidal component is given by $\boldsymbol{B}_{\rm pol} = B_r \boldsymbol{e}_r + B_z \boldsymbol{e}_z$, where $(\boldsymbol{e}_r, \boldsymbol{e}_\varphi, \boldsymbol{e}_z)$ are the cylindrical unit vectors.

Table 1. Comparison of growth rates obtained with FV (hybrid finite volume/boundary element method) and SFEMaNS. Rm is the magnetic Reynolds number, μ_r the disc permeability, γ_{m0}^t the growth rate of the axisymmetric toroidal field, γ_{m0} the growth rate of the axisymmetric mixed field and γ_{m1} the growth rate of the first non-axisymmetric field ($m1$-mode). The thickness of the impeller discs is $d = 0.1$.

Rm	μ_r	γ_{m0}^t	γ_{m0}	γ_{m1}	Scheme
0	1	-8.950	-4.159	-4.273	FV
0	1	-8.977	-4.162	-4.322	SFEMaNS
0	60	-1.292	-3.887	-1.715	FV
0	60	-1.305	-3.893	-1.722	SFEMaNS
30	1	-8.748	-3.591	-2.690	FV
30	1	-8.770	-3.597	-2.780	SFEMaNS
30	60	-1.134	-3.404	-2.511	FV
30	60	-1.155	-3.478	-2.476	SFEMaNS
70	1	-8.079	-3.467	-0.119	FV
70	1	-8.119	-3.471	-0.215	SFEMaNS
70	60	-1.203	-3.232	1.012	FV
70	60	-1.219	-3.264	0.969	SFEMaNS

et al 2008). Both approximation methods can account for insulating boundaries and non-uniform permeability and/or conductivity distributions. In the FV/BEM scheme, insulating boundary conditions are treated by solving an integral equation on the boundary, which allows a direct computation of the (unknown) tangential field components by correlating the (known) normal field components on the surface of the computational domain (Iskakov *et al* 2004, Giesecke *et al* 2008). In the SFEMaNS code, the magnetic field is computed numerically in a certain domain outside the cylinder and matching conditions at the interfaces with the insulator are enforced weakly by using an interior penalty technique (Guermond *et al* 2007).

The respective discretizations are done so that the transmission conditions across the material interfaces are satisfied[8]. In addition to their having passed independent convergence tests on manufactured solutions, the two codes have been cross-validated by comparing their outputs on various common test cases (see Giesecke *et al* (2010a, 2010c) and table 1).

We use the same configuration as that applied in Giesecke *et al* (2010b). The computational domain is inspired by the VKS configuration. The conducting fluid is contained in a cylinder of height $H = 2.6$ and radius $R_{out} = 1.4$, surrounded by an insulator. The fluid fills two unconnected compartments. The moving fluid is contained in an inner cylinder of radius $R_{in} = 1$.

---

[8] At the interface between two materials denoted by 1 and 2, the transmission conditions on the magnetic field and the electric field/current are given by

$$\boldsymbol{n} \cdot (\boldsymbol{B}^1 - \boldsymbol{B}^2) = 0 \quad \text{and} \quad \boldsymbol{n} \times \left(\frac{\boldsymbol{B}^1}{\mu_r^1} - \frac{\boldsymbol{B}^2}{\mu_r^2} \right) = 0 \quad \text{for permeability jumps and}$$

$$\boldsymbol{n} \cdot (\boldsymbol{j}^1 - \boldsymbol{j}^2) = 0 \quad \text{and} \quad \boldsymbol{n} \times (\boldsymbol{E}^1 - \boldsymbol{E}^2) = 0 \quad \text{for conductivity jumps.}$$

where $\boldsymbol{n}$ denotes the unit normal vector at the interface between both materials, $\boldsymbol{j}$ the current density and $\boldsymbol{E}$ the electrical field.

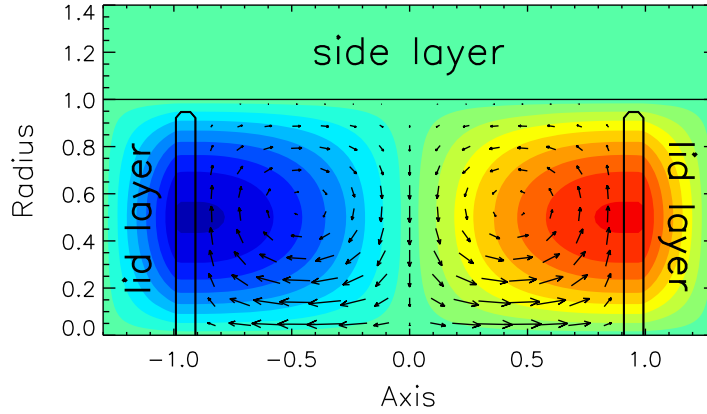**Figure 1.** Velocity field used in the kinematic simulations. The azimuthal velocity, u_φ, is shown in color and the poloidal component of the velocity, $u_r\boldsymbol{e}_r + u_z\boldsymbol{e}_z$, is shown with arrows. The black structures in the intervals $z \in [-1.0; -0.9]$ and $z \in [0.9; 1.0]$ represent two axisymmetric impellers of relative permeability $\mu_r > 1$. Note that the flow is mixed (poloidal and toroidal) between the two impeller discs and purely toroidal within and behind the impeller discs.

The fluid contained in the annular region comprised between the cylinders of radius $R_{in} = 1$ and $R_{out} = 1.4$ is at rest; this region is referred to as the side layer (see figure 1). Two discoidal subdomains of radius $R_{imp} = 0.95$ are located in the intervals $z \in [-1.0; -0.9]$ and $z \in [0.9; 1.0]$ and are meant to model soft iron impeller discs of thickness $d = 0.1$; the relative magnetic permeability in these two discs is denoted by μ_r. The velocity field $\boldsymbol{u}$ and the permeability distribution μ_r are assumed to be axisymmetric. The velocity field between the impeller discs in the inner cylinder is given by the so-called MND fluid flow (Marié *et al* 2006):

$$u_r(r, z) = -(\pi/h)\cos(2\pi z/h)\, r(1-r)^2(1+2r),$$
$$u_\varphi(r, z) = 4\epsilon r(1-r)\sin(\pi z/h),$$
$$u_z(r, z) = (1-r)(1+r-5r^2)\sin(2\pi z/h),$$

(3)

where h is the distance between the two impeller discs ($h = 1.8$) and ϵ parameterizes the toroidal to poloidal ratio of the flow (in the following we choose $\epsilon = 0.7259$)[9]. A purely azimuthal velocity equal to the azimuthal velocity of the MND flow at $z = \pm h/2$ is assumed in the two impeller discs. A so-called lid layer (Stefani *et al* 2006) is added behind each impeller disc, and the velocity field therein is modeled by linear interpolation along the z-axis between the azimuthal velocity at the outer side of the impeller disc and the no-slip condition at the lid of the vessel. The velocity field and the impeller discs (two thin structures shown with black solid lines) are displayed in figure 1. The conductivity is assumed to be uniform in the liquid metal and the soft iron discs. We focus in this paper on non-uniform permeability distributions only, which seems roughly justified for soft iron discs embedded in liquid sodium.

The equations are non-dimensionalized, so that $\mathcal{R} = R_{in}$ is the reference length scale (R_{in} is the radius of the flow active region) and $\mathcal{U} = \max[(u_r^2 + u_\varphi^2 + u_z^2)^{1/2}]$ is the reference velocity

---

[9] This value is close to the optimum relation between poloidal and toroidal flow that has been estimated in various comparable configurations (Ravelet *et al* 2005) and has frequently been utilized in previous studies of dynamo action driven by the MND flow (e.g. Stefani *et al* 2006, Gissinger *et al* 2008 and Giesecke *et al* 2010c).

scale (maximum absolute value of the velocity field). The control parameter is the magnetic Reynolds number defined by $Rm = \mu_0 \sigma \mathcal{U} \mathcal{R}$.

3. Results

The eigenvalues of the differential operator in the right-hand side of equation (1) are denoted by $\lambda = \gamma + i\omega$; the real part γ is the growth rate of the field amplitude ($\gamma < 0$ corresponds to decay) and the imaginary part ω is the frequency. All the computations reported below give non-oscillatory eigenmodes (i.e. $\omega = 0$). An immediate consequence of the axisymmetric setup is that the eigenmodes of the kinematic dynamo problem can be computed separately for each azimuthal wavenumber m.

3.1. Overview

We show in table 1 sample values of growth rates obtained by FV and SFEMaNS for the above simplified VKS model problem. This table confirms that FV and SFEMaNS converge to the same solutions up to 2% on the growth rates. We use the following notation in table 1 and in the rest of the paper: γ_{m0} is the growth rate of a mixed poloidal/toroidal mode. This mode degenerates to a purely poloidal mode when $Rm = 0$ and when there is no permeability jump (e.g. for stainless steel discs) this mode always determines the behavior of the axisymmetric field. Furthermore, γ_{m0}^{t} is the growth rate of the first axisymmetric mode ($m = 0$) that is purely toroidal and γ_{m1} is the growth rate of the first non-axisymmetric mode ($m = 1$).

When $Rm = 0$, the dominant and the second dominant $m0$-modes at $\mu_{r} = 1$ are purely poloidal and purely toroidal, respectively; the situation is reversed at $\mu_{r} = 60$: the dominant mode is purely toroidal. All growth rates increase with μ_{r}. When $Rm > 0$, the growth rate of the $m0$-mode is always negative in agreement with Cowling's theorem (Cowling 1933), but we observe that its relaxation time becomes longer as the permeability in the impeller discs increases. We also observe that dynamo action occurs on the $m1$-mode and that increasing μ_{r} lowers the critical threshold on Rm.

Snapshots of the dominant magnetic eigenmode are shown in figure 2. The structure of the $m1$-mode does not change very much with respect to μ_{r} and Rm; it is an equatorial dipole with two opposite axial structures mainly localized in the bulk of the fluid. In contrast, the $m0$-mode is essentially localized in the two impeller discs and barely differs from the pattern obtained in the free decay case (see figure 6).

3.2. Effect of the disc permeability on the m1-mode

Figure 3 shows the growth rate of the $m1$-mode as a function of the relative permeability of the impeller discs for four values of the Reynolds number. This figure is similar to figure 13a in Giesecke *et al* (2010c). The growth rate quickly reaches an asymptotic value when $Rm > 0$, which is not the case when $Rm = 0$. The $m1$-mode clearly depends on Rm and exhibits dynamo action when Rm is large enough. It can be seen in the left panel in figure 4 that the threshold for dynamo action goes from $Rm^{c} \approx 76$ when $\mu_{r} = 1$ to $Rm_{\infty}^{c} \approx 53.95$ when $\mu_{r} \to \infty$. The asymptotic threshold for $\mu_{r} \to \infty$ has been calculated by enforcing the boundary condition $\boldsymbol{H} \times \boldsymbol{n} = 0$ on the impeller discs (pseudo-vacuum or vanishing tangential field condition) while keeping the flow pattern (3) unchanged. This computation shows that, as far as the $m1$-mode
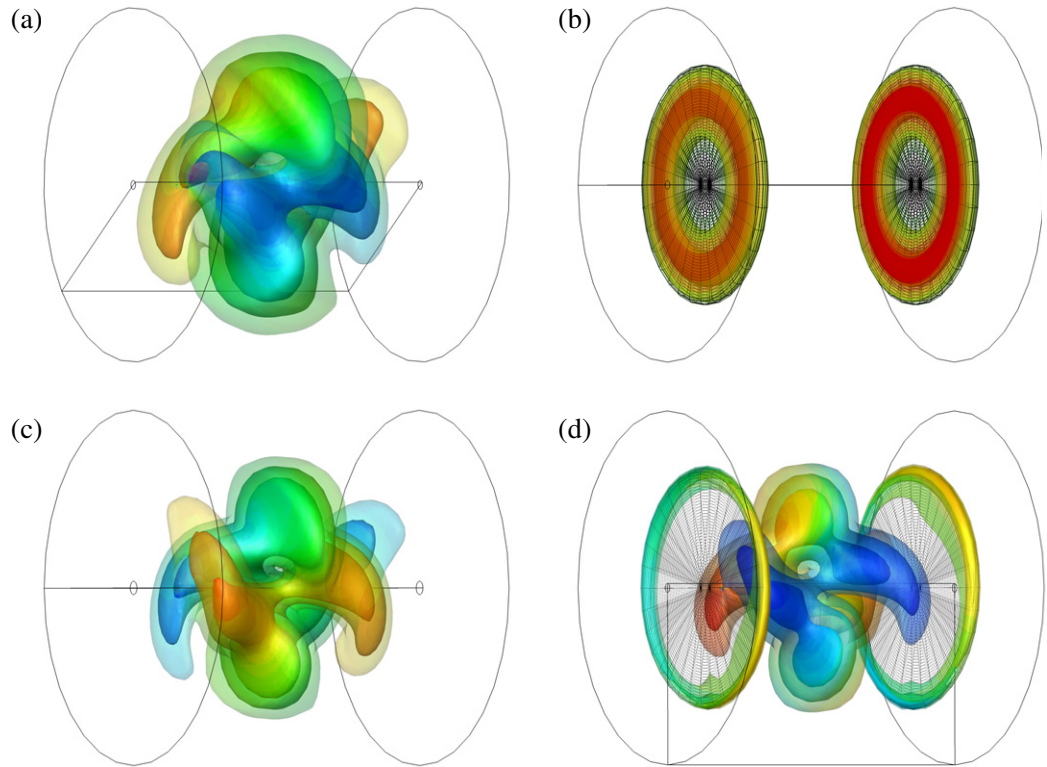
Figure 2. Dominant magnetic eigenmodes. The isosurfaces show the magnetic energy density at 10, 20 and 40% of the maximum value. The colors show $H_\varphi = \mu_r^{-1} B_\varphi$ and the meshes show the location of the soft iron discs (in the right column). Note that all eigenmodes are decaying except for the case $Rm = 70$, $\mu_r = 60$ (d), which is above the dynamo threshold and therefore presents a growing $m1$-mode. (a) $Rm = 30$, $\mu_r = 1$, $m = 1$, decay, (b) $Rm = 30$, $\mu_r = 60$, $m = 0$, decay, (c) $Rm = 70$, $\mu_r = 1$, $m = 1$, decay and (d) $Rm = 70$, $\mu_r = 60$, $m = 1$, growth.

is concerned, the impeller discs behave like an idealized ferromagnetic material in the limit $\mu_r \to \infty$. Upon inspection of the right panel in figure 4, where $Rm^c - Rm^c_\infty$ is displayed as a function of μ_r in log–log scale, we infer the following scaling law: $Rm^c - Rm^c_\infty \propto \mu_r^{-0.52}$. This type of scaling is an indication that a boundary layer effect is at play, which can be explained as follows. Starting with the idea that the stationary $m1$-dynamo is generated within the fluid flow, it is reasonable to expect that the rotating discs see this field as a quickly varying imposed field. The magnetic field cannot penetrate the discs when the permeability is infinite but, according to the classical skin effect, it can diffuse through a thin boundary layer of thickness $\delta = (\sigma \mu_r \Omega)^{-1/2}$ when μ_r is finite (Ω is the mean angular velocity). This diffusion effect adds a supplementary $\mu_r^{-1/2}$ damping to the magnetic field mode compared to the infinite permeability case.

3.3. Effect of the disc permeability on the m0-mode

Figure 5 shows the growth rates of the axisymmetric mode as a function of μ_r. Contrary to what we have observed for the $m1$-mode, the dependence of the $m0$-mode with respect to Rm
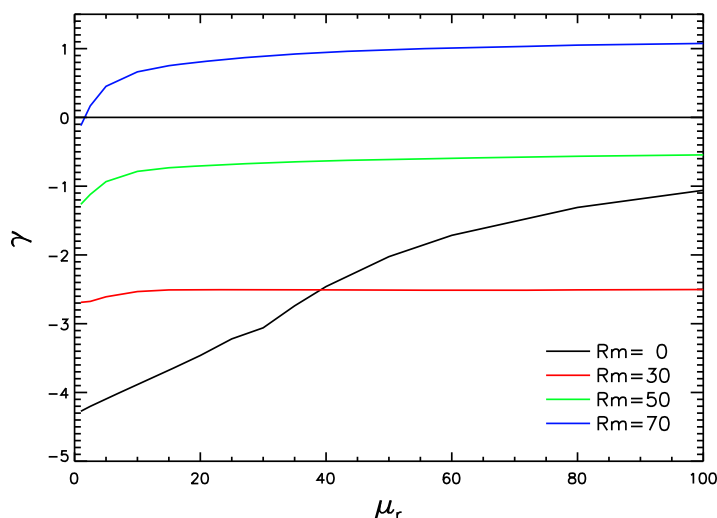
Figure 3. Growth rate of the $m1$-mode as a function of μ_r for $Rm = 0, 30, 50, 70$.
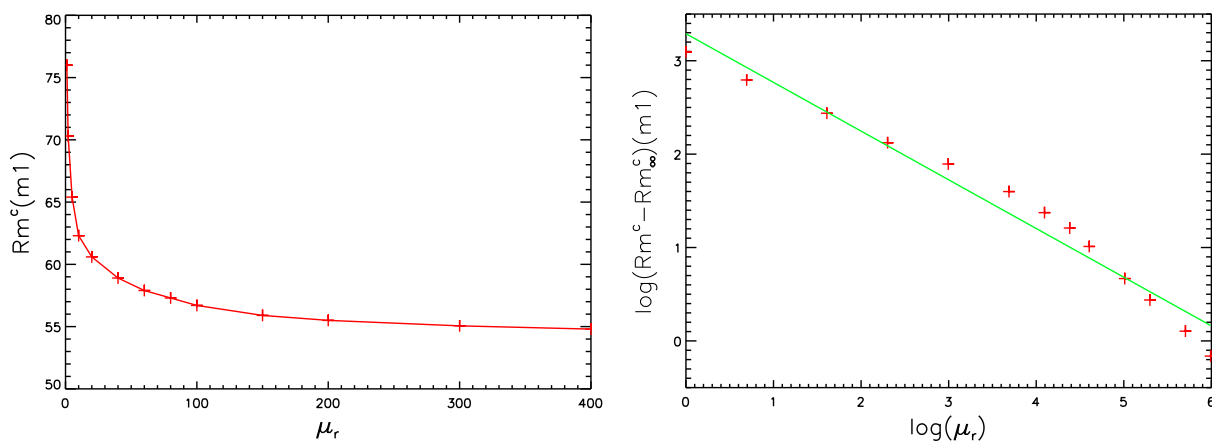

Figure 4. Left panel: dynamo threshold for the $m1$-mode as a function of μ_r. Right panel: a linear fit on log–log scale provides the scaling $Rm^c - Rm^c_\infty \propto \mu_r^{-0.52}$.

seems to be small; more precisely, the flow does not seem to play a significant role when the permeability is large.

In the free decay case ($Rm = 0$) the poloidal (dashed black line) and toroidal (solid black line) modes are decoupled and the growth rates of these two modes are $\gamma_{m0} = -4.159$ and $\gamma^t_{m0} = -8.950$, respectively. The decay time of the poloidal eigenmode is significantly larger than that of the toroidal one. The dominant poloidal eigenmode exhibits a typical dipolar pattern as shown in the left panel of figure 6. With increasing disc permeability (still at $Rm = 0$), the poloidal mode remains nearly unaffected (dashed black curve in figure 5), whereas the purely toroidal mode is significantly enhanced and eventually becomes dominant when $\mu_r \gtrsim \mu^t_r \approx 17.5$ (see solid curves in figure 5 and the right panel in figure 6). The growth rate of the toroidal mode increases monotonically with μ_r and roughly scales $\propto -\mu_r^{-1}$.

The introduction of a velocity field ($Rm > 0$) transfers poloidal field components into toroidal field components, but not vice versa. Therefore for increasing Rm a mixed mode is
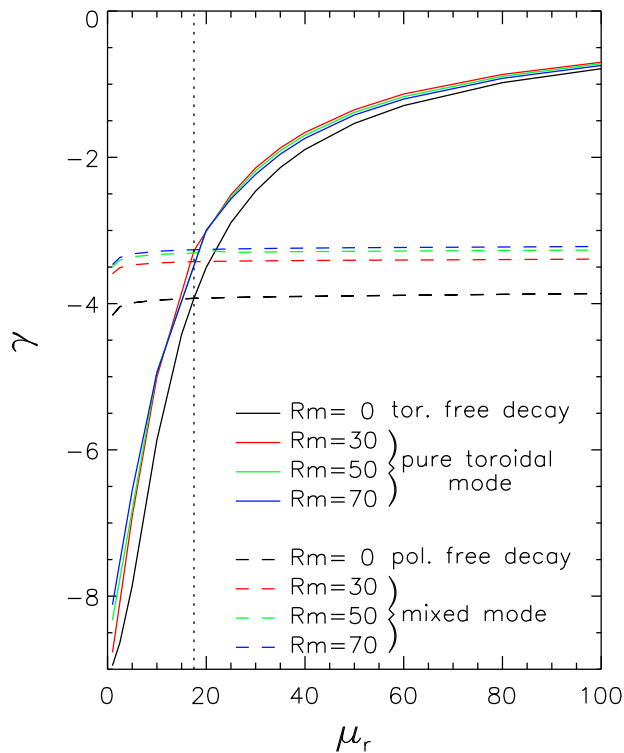
Figure 5. Growth rates of the $m0$-mode. The dotted vertical line marks the transitional value $\mu_r^t \approx 17.5$ at which the pure toroidal mode becomes dominant.
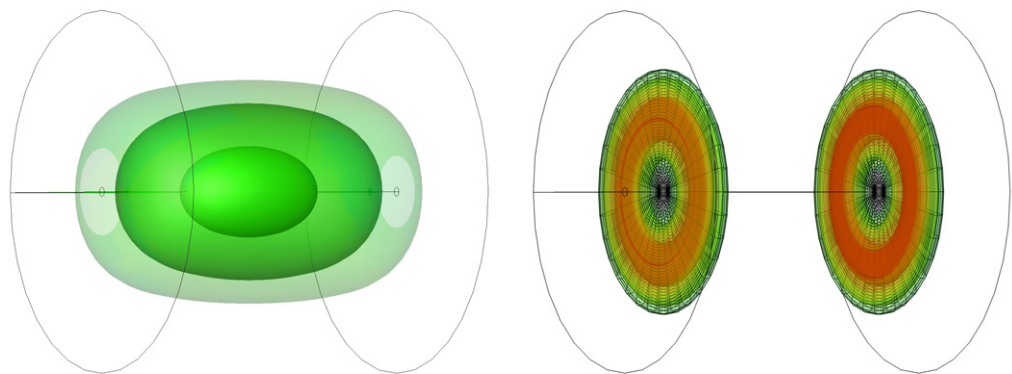

Figure 6. Spatial structure of the $m0$-mode in free decay ($Rm = 0$). Left panel: $\mu_r = 1$; right panel: $\mu_r = 60$. The isosurfaces show the energy density at 20, 40 and 80% of the maximum value. The colors code the azimuthal component $H_\varphi = \mu_r^{-1} B_\varphi$.

generated from the purely poloidal field that is observed at $Rm = 0$ (see dashed lines in figure 5). The dependence of the growth rate of the mixed mode with respect to the Reynolds number and the permeability is small. This mixed mode is dominant when $\mu_r \lesssim \mu_r^t$, but above this transitional point it is the purely toroidal eigenmode that dominates (see solid colored curves

in figure 5). The purely toroidal mode hardly depends on the magnetic Reynolds number and its growth rate increases with μ_r like in the free decay situation.

Surprisingly, the value of the transitional permeability μ_r^t is more or less the same for all the considered Reynolds numbers (see the vertical dotted line in figure 5 that marks the transition).

4. Discussion of the *m*0-mode

4.1. The coupling

Using the cylindrical coordinate system (r, φ, z) and assuming axisymmetry, the induction equation can be written as follows:

$$\left(\frac{\partial}{\partial t} + u_r \frac{\partial}{\partial r} + u_z \frac{\partial}{\partial z}\right) B_r = \left(B_r \frac{\partial}{\partial r} + B_z \frac{\partial}{\partial z}\right) u_r + \eta_0 \left[\frac{\partial}{\partial z}\left(\frac{\partial}{\partial z}\frac{B_r}{\mu_r} - \frac{\partial}{\partial r}\frac{B_z}{\mu_r}\right)\right], \tag{4}$$

$$\left[\frac{\partial}{\partial t} + u_r \left(\frac{\partial}{\partial r} - \frac{1}{r}\right) + u_z \frac{\partial}{\partial z}\right] B_\varphi = \left[B_r \left(\frac{\partial}{\partial r} - \frac{1}{r}\right) + B_z \frac{\partial}{\partial z}\right] u_\varphi + \eta_0 \Delta_* \frac{B_\varphi}{\mu_r}, \tag{5}$$

$$\left(\frac{\partial}{\partial t} + u_r \frac{\partial}{\partial r} + u_z \frac{\partial}{\partial z}\right) B_z = \left(B_r \frac{\partial}{\partial r} + B_z \frac{\partial}{\partial z}\right) u_z - \eta_0 \frac{1}{r}\frac{\partial}{\partial r}\left[r\left(\frac{\partial}{\partial z}\frac{B_r}{\mu_r} - \frac{\partial}{\partial r}\frac{B_z}{\mu_r}\right)\right], \tag{6}$$

where $\Delta_* = \frac{\partial^2}{\partial r^2} + \frac{1}{r}\frac{\partial}{\partial r} + \frac{\partial^2}{\partial z^2} - \frac{1}{r^2}$ and $\eta_0 = \frac{1}{\sigma \mu_0}$. This form of the induction equation clearly shows that $B_r = B_z = 0$ and $B_\varphi \neq 0$ can be an axisymmetric solution: this is the purely toroidal mode. If $B_r \neq 0$, $B_z \neq 0$, then their shearing by the non-zero azimuthal flow u_φ, the so-called Ω-effect, will always generate $B_\varphi \neq 0$, which then results in a mixed mode. The growth rate of the mixed mode will, however, remain entirely fixed by its poloidal components B_r and B_z (see figure 5).

Purely toroidal and purely poloidal fields cannot exist if μ_r depends on φ. The same remark holds if σ depends on φ; for instance, spatial variation of the electric conductivity is used in Busse and Wicht (1992) to produce dynamo action. However, when the permeability μ_r is axisymmetric there is no mechanism to transfer magnetic energy from the toroidal component B_φ to the poloidal pair (B_r, B_z) (see equations (4) and (6)).

4.2. Selective enhancement of B_φ

We start by explaining qualitatively why, for large values of μ_r, the purely toroidal mode is the least damped one and why the mixed mode is so little influenced by the disc. The argument is based on the paramagnetic pumping term (2) that is at the origin of an electromotive force (EMF):

$$\mathcal{E}^\mu = V^\mu \times B = \frac{1}{\mu_0 \mu_r \sigma}\frac{\nabla \mu_r}{\mu_r} \times B. \tag{7}$$

Since the permeability jump is restricted to the material interface there is only a contribution to the EMF within that localized area. For sufficiently thin discs, as considered here, it is reasonable to assume that the permeability jump at the rim of the impeller discs plays a minor role. We therefore assume that the pumping velocity is mainly axial: $V^\mu \propto \frac{\partial}{\partial z}\mu_r e_z$. The interaction of V^μ with the axial field $B_z e_z$ is henceforth neglected.

The interaction between $V^\mu \propto \frac{\partial}{\partial z}\mu_r e_z$ and the radial field $B_r e_r$ creates an azimuthal current $j_\varphi e_\varphi$ at the interface between the impeller discs and the fluid (see the left panel in figure 7). Since
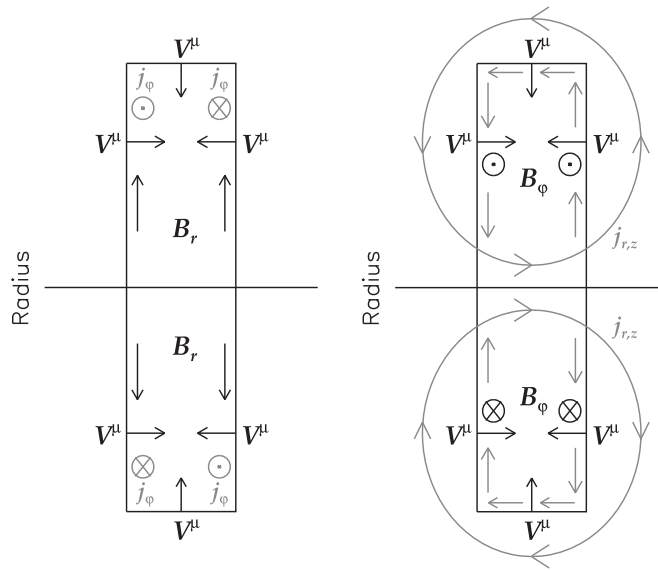
Figure 7. Left panel: current generation at the fluid–disc interface by paramagnetic pumping for a radial magnetic field B_r. Right panel: current generation from paramagnetic pumping for the azimuthal magnetic field B_φ.

the impeller discs are thin, it is reasonable to assume that the orientation and the amplitude of B_r do not change across the discs. This implies that the signs of the pumping term (2) at the back and at the front side of the discs are opposite, which in turn implies that the induced azimuthal currents mostly cancel each other and the overall azimuthal current is close to zero. This cancellation mechanism is weakened with thick discs. When the impeller discs are thick, the mixed mode and the purely toroidal mode have similar growth rates as can be observed in the left panels of figure 8 in Giesecke *et al* (2010c), where the above phenomenon is illustrated for two thicknesses of the impeller discs, $d = 0.1$ and $d = 0.6$.

The behavior is very different concerning the EMF that results from the interaction of the azimuthal component $B_\varphi e_\varphi$ with $\mathbf{V}^\mu$ (see the right panel in figure 7). In this case the currents generated at the front and at the back of the impeller discs add up and the EMF drives a poloidal current along the surface of the disc, which in turn re-enforces B_φ. Typical patterns of the EMF and current density from our numerical simulations are shown in figure 8. These graphics confirm the presence of the poloidal current and confirm also that the influence of the fluid flow is marginal.

4.3. Simplified model for the toroidal m0-mode

Our numerical results clearly indicate that the influence of the flow on the toroidal axisymmetric mode is negligible and that this mode is mostly localized inside the impeller discs. In order to better understand the dynamics of the toroidal $m0$-mode, we consider an idealized disc–fluid model in the free decay situation ($Rm = 0$).

Let us assume a disc of radius 1, permeability $\mu_r \gg 1$ and thickness d, sandwiched between two semi-infinite cylindrical fluid regions with $\mu_r = 1$. We further assume the boundary condition $\boldsymbol{H} \times \boldsymbol{n} = 0$ at the wall $r = 1$. This simplifying assumption will allow us to find
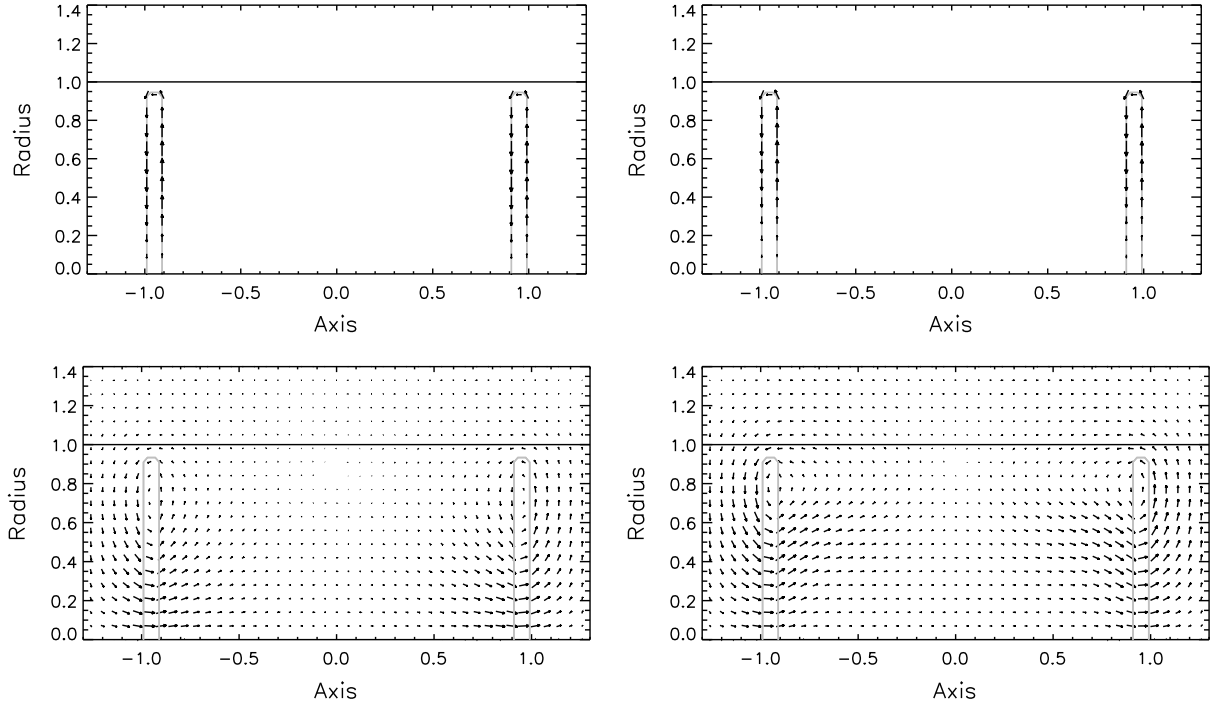
Figure 8. Paramagnetic pumping at $\mu_r = 60$. Upper row: EMF $\mathcal{E}^\mu = (\mu_0\mu_r\sigma)^{-1}\mu_r^{-1}\nabla\mu_r \times B_\varphi\mathbf{e}_\varphi$ at $Rm = 0$ (left) and $Rm = 30$ (right). Lower row: (poloidal) current density $\boldsymbol{j} = (\mu_0)^{-1}\nabla \times \boldsymbol{B}/\mu_r$ at $Rm = 0$ (left) and $Rm = 30$ (right). The light gray lines show soft iron discs and the solid horizontal line shows the separation between the moving fluid and the stagnant side layer. The azimuthal current is negligible. Note the close similarity between free decay (left column) and the case $Rm = 30$ (right column) illustrating the marginal impact of the fluid flow.

analytical solutions. We solve

$$\mu_r\gamma B_\varphi = \Delta_* B_\varphi, \qquad r < 1, \qquad |z| < d/2,$$
$$\gamma B_\varphi = \Delta_* B_\varphi, \qquad r < 1, \qquad |z| > d/2, \tag{8}$$

where $\Delta_* = \frac{\partial^2}{\partial r^2} + \frac{1}{r}\frac{\partial}{\partial r} + \frac{\partial^2}{\partial z^2} - \frac{1}{r^2}$. Note that the non-dimensionalization is done so that the reference scale of the growth rate is $(\sigma\mu_0 R^2)^{-1}$. The boundary condition is $B_\varphi = 0$ at $r = 1$, and the transmission condition across the material interface is that H_φ and $E_r = \partial_z H_\varphi/\sigma$ be continuous at $z = \pm d/2$.

The numerical simulations show that the dominating eigenmodes are symmetric with respect to the equatorial plane of the disc $z = 0$. This leads to the following ansatz:

$$B_\varphi = A_1 J_1(kr)\cos l_1 z, \quad r < 1, \quad 0 < z < d/2,$$
$$B_\varphi = A_2 J_1(kr)\,e^{-L_2 z}, \quad r < 1, \quad z > d/2,$$

where J_1 is the Bessel function of the first kind and

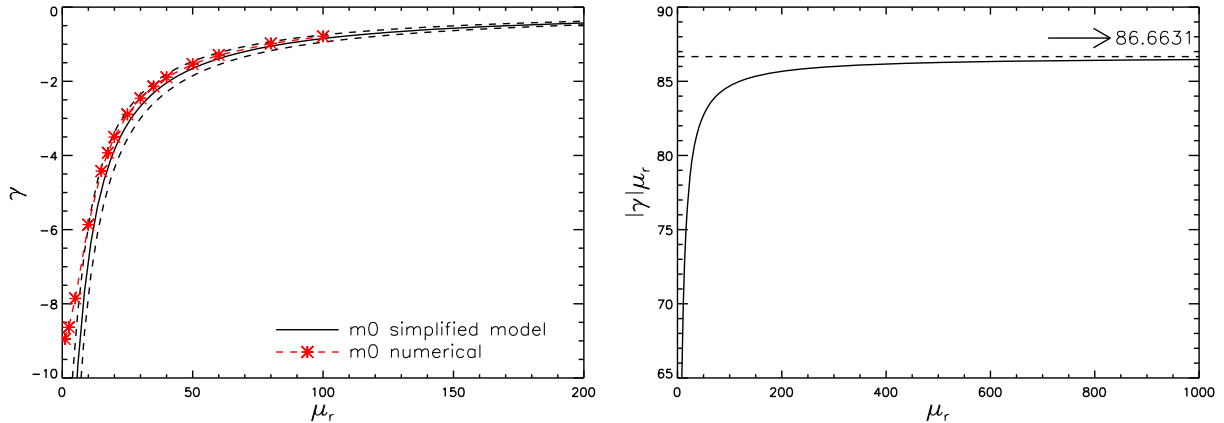$$l_1 = \sqrt{-\gamma\mu_r - k^2}, \quad L_2 = \sqrt{k^2 + \gamma}. \tag{9}$$

Figure 9. Left: growth rate γ as a function of μ_r for the dominant axisymmetric toroidal eigenmode from the numerical model and the simplified model with $d = 0.1$, $k = k_1$ and $k = (1 \pm 0.1)k_1$. Right: using the proper time scale $\sigma \mu_r \mu_0 R^2$ involving the permeability of the impeller disc, the growth rate $\tilde{\gamma} = \gamma \mu_r$ reaches an asymptote at high μ_r.

The amplitudes A_1 and A_2 are arbitrary for the moment. The fields are obtained by symmetry for $z < 0$. To ensure that the solution decays at infinity (i.e. it remains bounded when $z \to \pm\infty$), it is necessary that l_1 and L_2 be real. This imposes the constraints

$$\mu_r > 1, \quad \gamma \in [-k^2, -k^2/\mu_r]. \tag{10}$$

The boundary condition at $r = 1$ implies that $J_1(k) = 0$, i.e. k is a zero of J_1. We choose the first zero, say k_1, so that the solution is composed of one radial cell only,

$$k_1 \approx 3.8317. \tag{11}$$

This value specifically depends on the idealized boundary condition that we have assumed at $r = 1$; the effect of small deviations $k = (1 \pm 0.1)k_1$ is considered further below. Due to the assumed symmetry, we need to impose the transmission conditions at the $z = d/2$ interface only:

$$\left(\frac{1}{\mu_r} \cos \frac{l_1 d}{2}\right) A_1 - \left(e^{-L_2 d/2}\right) A_2 = 0,$$

$$\left(\frac{l_1}{\sigma \mu_r} \sin \frac{l_1 d}{2}\right) A_1 - \left(\frac{L_2}{\sigma} e^{-L_2 d/2}\right) A_2 = 0. \tag{12}$$

The determinant of the above linear system must be zero for a solution to exist,

$$L_2 \cos \frac{l_1 d}{2} - l_1 \sin \frac{l_1 d}{2} = 0. \tag{13}$$

Upon inserting the definitions of l_1 and L_2 from (9) into this dispersion relation, we obtain an implicit nonlinear equation for the growth rate γ as a function of d and μ_r.

We show in the left panel of figure 9 the graph of the function $\gamma(\mu_r)$ deduced from (13) with $d = 0.1$ and $k = k_1 = 3.8317$. Two further analytical graphs computed with $k = (1 \pm 0.1)k_1$ show the very weak sensitivity of the growth rate on relaxing the strict boundary condition $H \times n = 0$ (e.g. by using an outer shell of a different conductivity). We also show in this figure

the numerical outcome for the growth rate of the purely toroidal mode at $Rm = 0$ (see also the black solid line in figure 5). The agreement is quite satisfactory and thereby confirms our analysis. When representing $\gamma(\mu_{\rm r})$ in log–log scale (not shown) we see that $\gamma(\mu_{\rm r})$ scales like $\mu_{\rm r}^{-1}$ in the limit $\mu_{\rm r} \to \infty$. Actually this behavior depends on the choice that we have made for the non-dimensionalization. Involving the disc's permeability for defining the new time scale $(\sigma \mu_{\rm r} \mu_0 R^2)$ instead of $(\sigma \mu_0 R^2)$, we obtain the rescaled growth rate $\tilde{\gamma} = \gamma \mu_{\rm r}$ shown in the right panel of figure 9. This representation shows that the growth rate $\tilde{\gamma}$ reaches a constant value for very high permeabilities ($\tilde{\gamma}_\infty = -86.6631$). This observation immediately implies that the following power law, $\gamma \sim \tilde{\gamma}_\infty/\mu_{\rm r}$, holds in the original units when $\mu_{\rm r} \to +\infty$.

In conclusion, the above simplified model explains why the growth rate of the purely toroidal mode goes to zero when $\mu_{\rm r} \to \infty$. The model shows also that although the dominant purely toroidal mode is localized to a very small volume, its decay time determines the overall decay of the axisymmetric azimuthal magnetic field. Note, finally, that this mode would not be observed in numerical simulations of VKS dynamos that use the idealized boundary condition $\boldsymbol{H} \times \boldsymbol{n} = 0$ on the disc's surface (see, e.g., Gissinger *et al* (2008)).

5. Conclusions

The aim of this paper is to study the influence of thin high-permeability discs on a VKS-like dynamo model. This work goes well beyond the study of Giesecke *et al* (2010c) in the sense that we investigate thoroughly the axisymmetric mode and present novel details of the scaling behavior of the dynamo $m1$-mode. The high-permeability discs facilitate the occurrence of non-axisymmetric dynamo action by enhancing the growth rate of the equatorial dynamo $m1$-mode. Compared to the idealized limit ($\mu_{\rm r} \to \infty$) the presence of a finite but high permeability material adds a small supplementary damping effect and therefore slightly increases the dynamo threshold. We propose that the observed $\mu_{\rm r}^{-1/2}$-scaling for the dynamo threshold can be explained by a skin-effect so that the disc's role in the $m1$-mode is quite passive. Although the reduction of the magnetic Reynolds number is substantial (from $Rm^{\rm c} \approx 76$ at $\mu_{\rm r} = 1$ to $Rm^{\rm c} \approx 54$ in the limit $\mu_{\rm r} \to \infty$) the spatial structure of the $m1$-mode is hardly changed.

The effects of the high permeability of the impeller discs on the axisymmetric mode turn out to be more fundamental. In the presence of a mean flow, the axisymmetric $m0$-modes are split into two separate families, one consisting of a purely toroidal mode and one consisting of a mixed mode composed of a poloidal and a toroidal component. The growth rate of the mixed $m0$-mode slightly increases with Rm but is nearly independent of the disc permeability. The growth rate of the purely toroidal $m0$-mode is not significantly influenced by the flow amplitude, but it is considerably enhanced $\propto \mu_{\rm r}^{-1}$ for large values of $\mu_{\rm r}$. This selective enhancement of the purely toroidal $m0$-mode can be explained qualitatively by paramagnetic pumping. A simplified analytical model that interprets the purely toroidal mode as a localized free decay solution confirms the scaling obtained in the numerical simulations. This slowly decaying purely toroidal mode promoted through the high-permeability discs may play an important role in axisymmetric dynamo action. However, in our simple axisymmetric setup no possibility for a closure of the dynamo cycle is provided since the poloidal component remains decoupled from the dominant toroidal field, so that such a dynamo remains impossible (Cowling 1933, Hide and Palmer 1982).

Our study shows that the ideal boundary conditions $\boldsymbol{H} \times \boldsymbol{n} = 0$ are indeed a reasonable assumption for the $m1$-mode, but are not appropriate for the analysis of the toroidal

$m0$-mode. The purely toroidal $m0$-mode can be obtained only by explicitly considering the internal permeability distribution and the corresponding jump conditions at the fluid/disc interface. This mode cannot be obtained numerically by simulations of VKS-like dynamos that use either the idealized boundary condition $\boldsymbol{H} \times \boldsymbol{n} = 0$ at the fluid/disc interface or the thin-wall approximation from Roberts *et al* (2010).

In conclusion, we have seen that the high (but finite) permeability in the impeller discs is very important to promote axisymmetric modes in our model and we suppose that it may also play a non-trivial role in the real VKS experiment. For example, in the presence of more complex (non-axisymmetric) flows containing small-scale turbulence modeled by an α-effect (Laguerre *et al* 2008, Giesecke *et al* 2010a) or in the presence of non-axisymmetric permeability distributions that resemble the soft-iron blades attached to the discs (Giesecke *et al* 2010b), the purely toroidal $m0$-modes can be coupled with poloidal field components, thus providing the required mechanism to close the dynamo loop.

Acknowledgments

References

Busse F H and Wicht J 1992 *Geophys. Astrophys. Fluid Dyn.* **64** 135–44
Cowling T G 1933 *Mon. Not. R. Astron. Soc.* **94** 39–48
Dobler W, Frick P and Stepanov R 2003 *Phys. Rev.* E **67** 056309
Dudley M L and James R W 1989 *Proc. R. Soc.* A **425** 407–29
Giesecke A, Stefani F and Gerbeth G 2008 *Magnetohydrodynamics* **44** 237–52
Giesecke A, Nore C, Plunian F, Laguerre R, Ribeiro A, Stefani F, Gerbeth G, Léorat J and Guermond J 2010a *Geophys. Astrophys. Fluid Dyn.* **104** 249–71
Giesecke A, Stefani F and Gerbeth G 2010b *Phys. Rev. Lett.* **104** 044503
Giesecke A, Nore C, Stefani F, Gerbeth G, Leorat J, Luddens F and Guermond J 2010c *Geophys. Astrophys. Fluid Dyn.* **104** 505–29
Gissinger C, Iskakov A, Fauve S and Dormy E 2008 *Europhys. Lett.* **82** 29001
Guermond J L, Laguerre R, Léorat J and Nore C 2007 *J. Comput. Phys.* **221** 349–69
Guermond J L, Léorat J, Luddens F, Nore C and Ribeiro A 2011 *J. Comput. Phys.* **230** 6299–319
Hide R and Palmer T N 1982 *Geophys. Astrophys. Fluid Dyn.* **19** 301–9
Iskakov A B, Descombes S and Dormy E 2004 *J. Comput. Phys.* **197** 540–54
Krause F and Rädler K H 1980 *Mean-Field Magnetohydrodynamics and Dynamo Theory* (Oxford: Pergamon)
Laguerre R, Nore C, Ribeiro A, Léorat J, Guermond J and Plunian F 2008 *Phys. Rev. Lett.* **101** 104501
Lowes F J and Wilkinson I 1963 *Nature* **198** 1158–60
Lowes F J and Wilkinson I 1968 *Nature* **219** 717–8
Marié L, Normand C and Daviaud F 2006 *Phys. Fluids* **18** 017102
Monchaux R *et al* 2009 *Phys. Fluids* **21** 035108
Monchaux R, Berhanu M, Bourgoin M, Moulin M, Odier P, Pinton J F, Volk R, Fauve S, Mordant N and Pétrélis F 2007 *Phys. Rev. Lett.* **98** 044502

Ravelet F, Chiffaudel A, Léorat J and Daviaud F 2005 *Phys. Fluids* **17** 117104

Roberts P H, Glatzmaier G A and Clune T L 2010 *Geophys. Astrophys. Fluid Dyn.* **104** 207–20

Stefani F, Xu M, Gerbeth G, Ravelet F, Chiffaudel A, Daviaud F and Léorat J 2006 *Eur. J. Mech.* B **25** 894–08

Verhille G, Plihon N, Bourgoin M, Odier P and Pinton J 2010 *New J. Phys.* **12** 033006

Wicht J and Busse F H 1993 *Solar and Planetary Dynamos* ed M R E Proctor, P C Matthews and A M Rucklidge (Cambridge: Cambridge University Press) pp 329–37